

# 3D Bulk Ordering in Macroscopic Solid Opaline Films by Edge-Induced Rotational Shearing

Chris E. Finlayson,\* Peter Spahn, David R. E. Snoswell, Gabrielle Yates, Andreas Kontogeorgos, Andrew I. Haines, G. Peter Hellmann, and Jeremy J. Baumberg\*

A breakthrough in the field of large area photonic structures is reported, based on permanent ordering of solid polymeric films of sub-micrometer spheres by edge rotational-shearing. The resulting high-quality polymer opal thin-films exhibit strikingly intense structural color, as confirmed by combining a number of spectroscopic approaches. This induced self-assembly on macroscopic length scales represents a step-change away from current surface lithographies, presenting new routes for assembling solid ordered photonic materials. Despite previous reports of shear-ordering in sedimentary colloids in solution,<sup>[1,2]</sup> no precedents exist for the application of such techniques to these granular solvent-free systems, which allow formation of permanent composite structures in the solid-state.

Full 3D ordering of sub-micrometer components into defined architectures is a major challenge for bottom-up nanophotonics, nano-electronics, plasmonics and metamaterials.<sup>[3–5]</sup> Even simple structures, such as opaline photonic crystals based on fcc colloidal lattices, have optical properties dominated by defects and cannot be fabricated in any scalable fashion.<sup>[6–9]</sup> Here, we report a significant advance in high-quality polymer opal thin-films exhibiting tunable structural color across visible wavelengths. An edge-induced rotational shearing (EIRS) process produces reproducible highly uniform samples with bulk-ordering of sub-micrometer components, greatly enhancing both the intensity and chromaticity of the observed structural color. The demonstration of reproducible scale-up of these elastomeric synthetic opaline films to industrial length scales makes them very attractive as a route to a wide range of large-area photonics applications, including sensors and coatings<sup>[10]</sup> as well as metamaterials when combined with metallic core-shell particles.

The advance reported here is based on a recently developed technique to produce flexible opals using melting and shear-ordering under compression of core/shell polymer nanoparticles.<sup>[11–13]</sup> So far, this produces flexible polymer opals with fundamental optical resonances tunable across the visible and

near-infrared regions (by varying the precursor nanosphere size from 200–350 nm and hence the resulting fcc lattice parameter). In the low-refractive-index contrast regime associated with these polymer composites, color generation arises through spectrally resonant scattering inside a 3D fcc-lattice photonic crystal,<sup>[14,15]</sup> as opposed to normal reflective iridescence based on Bragg diffraction. Additionally, the introduction of a small fraction of carbon nanoparticle pigment into the interstices of the photonic crystal lattice does not disrupt the lattice quality, but results in a remarkable increase in the color saturation of the opals with the concentration of carbon.<sup>[11–15]</sup> This principle is of fundamental interest in understanding the origins of structural colors and iridescence in natural opals, such as those in minerals or in biological structures.<sup>[16]</sup> However, the main difficulty of this fabrication approach has been the lack of true bulk order, and it is this advance that is reported below.

The polymeric opal system described in this paper is based on ensembles of core–interlayer–shell (CIS) particles synthesized by an emulsion polymerization process.<sup>[17,18]</sup> Rigid cross-linked polystyrene spheres are capped by a soft polyethylacrylate (PEA) shell, via an interlayer containing allyl-methacrylate (ALMA) as a grafting agent (Figure 1a). The net refractive index contrast between the core and shell material is  $\Delta n \approx 0.11$ . A full description of the process, which consists of a combination of extrusion, rolling (linear shear), and edge-induced rotational shearing processes yielding permanent rolls of opal films (Figure 1b), is given in the Experimental Section. The resultant opaline samples are observed to have a brilliant visual iridescence (Figures 1e–h), which markedly improves during the edge-shear step. These images also illustrate how this iridescence is readily tunable, both with the size and spacing of the core particles (the green opal has a base core diameter of  $\approx 215$  nm; for the red opal, this diameter is 250 nm) and also with the angle of viewing. EIRS induces ensembles of the CIS polymer particles to form highly ordered opaline structures under the melt conditions at 150 °C (Figure 1d), which this paper aims to characterize and understand.

A spectroscopic study of typical green opal samples shows a clear enhancement of both bright- and dark-field reflectance after EIRS (Figure 2). For consistency, we concentrate below on green opal films with 0.05 wt% carbon nanoparticle loading, unless otherwise stated. In such a photonic crystal medium of relatively low refractive index contrast, resonant backwards scattering (in dark-field) enhanced by the carbon nanoparticles is stronger than the normal incidence reflection (bright-field). The chromaticity of reflected light from green opal samples (Supporting Information, Figure S1) on the Commission Internationale de l'Éclairage (CIE) color space shows that the EIRS

Dr. C. E. Finlayson, Dr. D. R. E. Snoswell, G. Yates, A. Kontogeorgos, A. I. Haines, Prof. J. J. Baumberg  
NanoPhotonics Centre  
University of Cambridge  
Cambridge CB3 0HE, UK  
E-mail: cef2@aber.ac.uk; jjb12@cam.ac.uk

Dr. P. Spahn, Dr. G. P. Hellmann  
Deutsches Kunststoff-Institut (DKI)  
Schlossgartenstrasse 6, D-64289 Darmstadt, Germany

DOI: 10.1002/adma.201003934

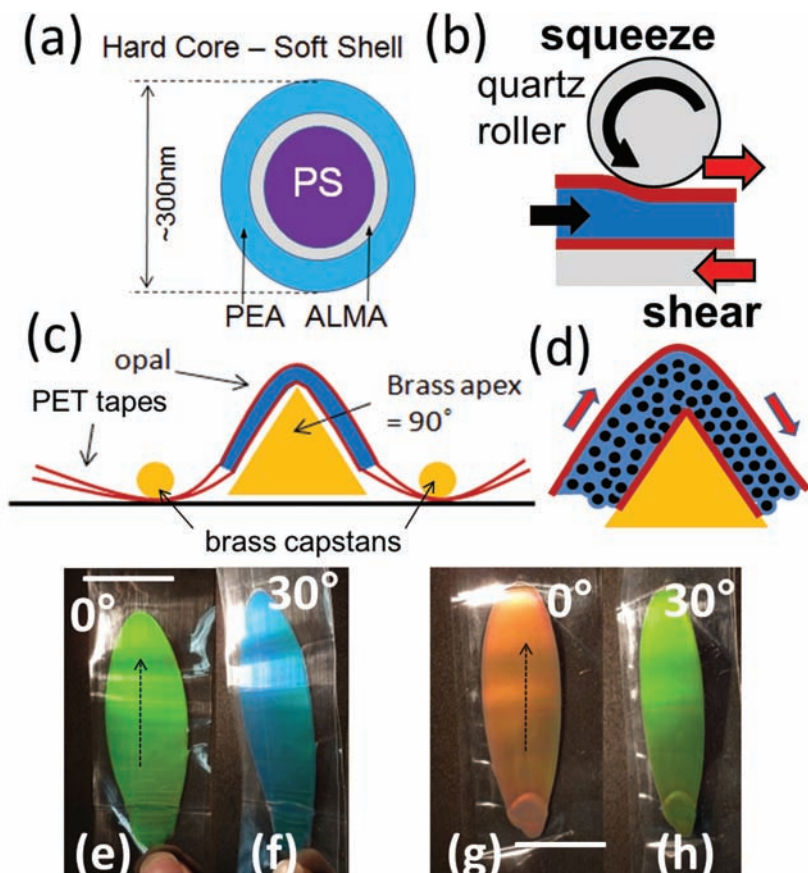


**Figure 1.** a) CIS of the constituent particles used in polymer opals. b) Schematic of the roller process producing 100- $\mu\text{m}$ -thick opal films via squeeze/linear shear. c) Schematic of hot-edge process, exploiting edge-shearing mechanism as illustrated in (d). See Experimental Section for more detail. e, f) Photographs of a processed green opal sample viewed in reflected white-light at angles of e)  $0^\circ$  and f)  $30^\circ$  to the normal. g, h) Corresponding images of a red opal sample. Arrows in (e, g) show direction of edge-shear processing, scale bars are 3 cm.

process produces near-saturated colors (of 20-nm linewidth, compared to pure monochromes at the CIE edge) from the initial samples of near-white chromaticity (at the CIE center). This enhancement in perceived color is also vividly demonstrated in the images in Figure 2a (inset).

While the reflectivity spectra imply opaline ordering within the optical depth of the samples, typically  $<20 \mu\text{m}$ ,<sup>[14]</sup> a better indication of bulk ordering is given by the optical transmittance spectra (Figure 2b). Before EIRS, we observe a featureless spectrum characterized by decreasing transmittance at short wavelengths, as expected from an ensemble of scattering centers with poor structural ordering.<sup>[19]</sup> Visually, such samples appear dark orange in transmitted light, with little or no variation with viewing angle. There is a dramatic change after the EIRS process, with a pronounced minimum in the transmission spectrum corresponding to the resonant wavelength of a bulk-ordered array of scatterers, the width of this resonance being determined by the resultant photonic stop-band. Commensurately, the edge-sheared samples show a very marked visual complementary color effect when viewed in transmission, which is also strongly tunable with viewing angle (Figure 2b, inset).

Lateral cross sections of the films taken at  $30^\circ$  to the shear-direction show near-resonant (111)-plane optical scattering allowing the study of ordering at different depths within the films (Supporting Information, Figure S2). Previous compression processing of opal thin-films from the as-extruded CIS bulk material via squeeze-shear<sup>[13,14]</sup> had the drawback that the opals were formed of discrete well-ordered surface layers and a poorly ordered interior (Supporting Information, Figure S2c). Hence these previous samples show weaker structural color and virtually no effect in transmittance due to the lack of uniform bulk ordering. By contrast, cross-sectional dark-field images of the current samples (Supporting Information, Figures S2a, b) already show no obvious signs of any layering after the first linear shear process. Hence, the uniformity present in the sample before the EIRS process is also maintained in the final highly ordered sample.

To demonstrate the 3D bulk ordering achieved in these opaline films, optical diffraction experiments were performed on large sphere films in transmittance. For samples where the core spacing of the opal was larger than the wavelength,  $\lambda = 404 \text{ nm}$ , of the laser source, this readily revealed very clear and distinctive diffraction-spot patterns, with a characteristic sixfold symmetry (Figure 3a), which was precisely aligned to the flow direction in the EIRS process at every location on the sample films. Based upon the measured angle of diffraction of  $54^\circ$ , the planar spacing of the fcc-lattice (111) plane was calculated to be around 500 nm, in good agreement with expectation for spheres of spacing  $\approx 630 \text{ nm}$ . The interpretations of these experiments are threefold; firstly, the appearance of such well-resolved diffraction spots in transmission for the edge-sheared sample represents compelling evidence of a monodomain crystalline structure throughout the film of many hundred sphere layers. Secondly, a very significant sharpening of the diffraction spots is found upon edge-shearing these films (Figure 3a), giving a further indication of the improved ordering following the EIRS process. Thirdly, simple (single scattering) models of diffraction in the case of a perfectly ordered fcc symmetry predict three spots in reciprocal space.<sup>[20]</sup> However, the consistent appearance of six spots of equal intensity has recently been shown to arise from the complicated diffraction within the 3D photonic crystal fcc geometry.<sup>[21]</sup> We note that this pattern can also arise from even a single stacking fault within the bulk-ordered structure;<sup>[22]</sup> the exact nature and spatial distribution of faults leading to twinning are under further investigation.

To better understand the role of EIRS on the ordering within the polymer opal system, we consider the motion of subvolumes within the film (of initial thickness  $t$ ) that are rigidly stuck to the outer polyester (PET) tape sheets (Figure 3b). This model of rigid outer sheets with a fluid core shows how the bending

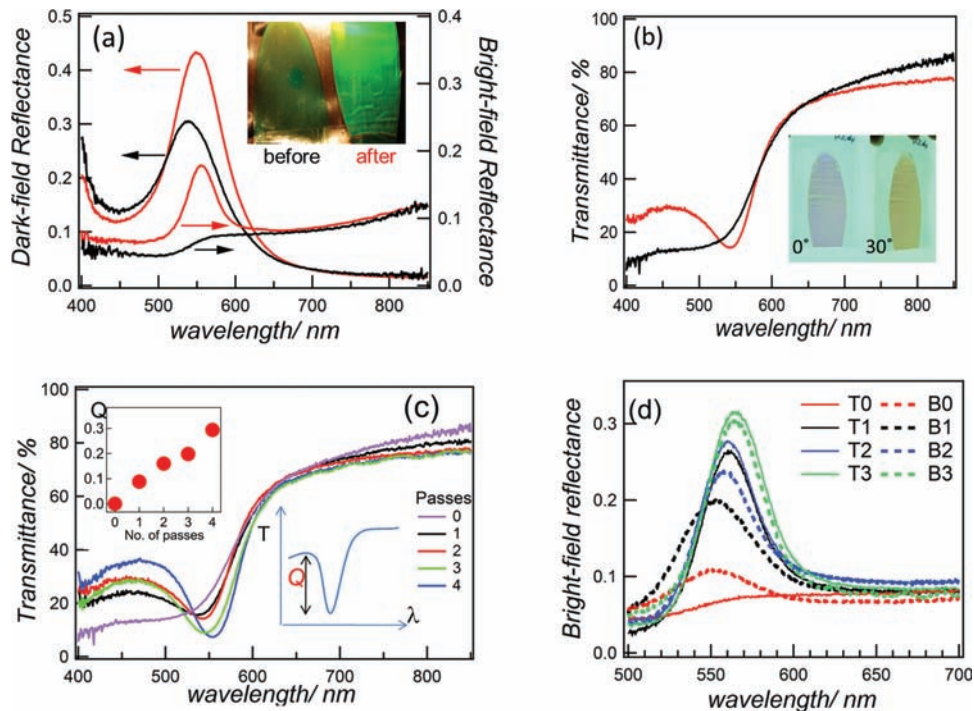


**Figure 2.** a) Dark- and bright-field normal incidence reflectivity for a green opal thin-film before (black) and after (red) a single-pass edge-shear. Inset: raw photos in reflected white light of the edge-sheared opal film (right) and the presheared film (left). b) Transmission spectra for 100- $\mu\text{m}$ -thick films. Inset: photo with white-light back illumination of edge-sheared opal film, viewed at  $0^\circ$  (left) and  $30^\circ$  (right) to the normal. c) Transmission spectrum of green opaline films as a function of the number of edge-shearing passes at  $5 \text{ mm s}^{-1}$ , compared to a 100- $\mu\text{m}$ -thick film before shearing. Inset: sample quality,  $Q$ , vs number of passes. d) Bright-field reflectance spectra of the top (T) and bottom (B) surfaces as the number of passes is increased.

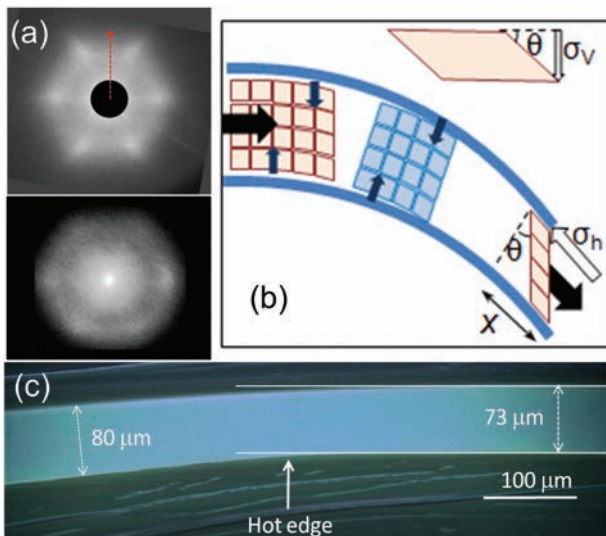


**Figure 3.** a) Transmission diffraction pattern taken at normal incidence for an  $\approx 40\text{-}\mu\text{m}$ -thick film of an edge-sheared opal with sphere diameter of 630 nm (top). The sample edge-shearing direction relative to the pattern is indicated with an arrow. A clear difference in the pattern can be seen between films with and without (bottom) edge-shearing. b) Schematic of bend-induced shearing (blue arrows) of opal between rigid PET films passed over edge, developing horizontal shear strain ( $\sigma_h$ ) and vertical shear strain ( $\sigma_v$ , upper inset) perpendicular to processing direction. c) Microscope image ( $\times 20$ , dark-field) of green-opal film in cross-section transverse to the edge-shear processing direction, during edge-shear process (edge stopped at point indicated).

rotation of the opal at the hot-edge (apex angle  $\alpha = 90^\circ$  and radius of curvature  $< 10 \mu\text{m}$ ) produces a vertical shear strain,  $\sigma_v$ , (as opposed to the applied lateral shear strain,  $\sigma_h = \alpha$  in radians), whose orientation rotates as the subvolumes follow the top and bottom sheets. From the net shear of the films relative to each other over the bending edge, we predict a thinning of the opal film, depending on the bending angle after the film relaxes,  $\theta$ . This thinning is revealed by measuring the cross-section of an opal film parallel to the processing direction (Figure 3c), which has been stopped with the hot-edge at the point indicated. The thinning profile indeed resembles the model in Figure 3b, and the thickness of the opal film decreases by  $\Delta t/t = 9\%$ . We note that in the ideal case, the lateral shear would produce a thinning  $\Delta t/t = 1 - \cos[\tan^{-1}(\alpha)] = 47\%$ , hence there is currently a degree of slip within the apparatus. The measured thinning corresponds to a bending angle  $\theta = \cos^{-1}(1 - \Delta t/t) = 24^\circ$  and a net vertical strain of  $\sigma_v = \tan(\theta) = 46\%$ . This level of strain in the sample is significant, as it exceeds the critical yield strain beyond which the lattice planes in the opal are found to start slipping past each other, at 25% shear strain.<sup>[13]</sup> This observed yield strain is in good agreement with that expected for a perfect fcc hard-sphere model.<sup>[23,24]</sup> Optical diffraction measurements show that the shear-processing direction completely sets the [110] close-packed orientation of the hexagonal lattice,<sup>[12,24]</sup> with the (111) plane remaining parallel to the top sample surface despite the rotating vertical shear. We also observe up to 3% red-shift of the Bragg peak after several passes (Figure 2a) as the layers become better packed when ordered. Within the

viscoelastic regime of the CIS ensemble, such a slipping and relaxation process provides a mechanism for the core particles to be reconfigured towards a fully crystalline ordering. The role of the edge-induced rotational-shear geometry is to provide a controllable fixed shear strain (but not shear flow) for each point in the film, as we previously showed is critical for ordering.<sup>[24]</sup> We suggest that shear strains of 40% favor the fcc lattice by concentrating shear forces along close-packed directions towards the walls: defects in these close-packed directions (from domains of hexagonal- or random-close packing) yield first, selectively annealing them out and providing a mechanism for beyond-nearest-neighbor hard-sphere interactions (Monte-Carlo simulations underway aim to confirm this hypothesis).<sup>[25]</sup> Controlling the shear strain using the hot edge process has the advantage that the rate of shearing can be kept well below the threshold for shear melting<sup>[13]</sup> above which all sample properties rapidly degrade. As a further confirmation of the EIRS mechanism, concentric holes made through the top and bottom PET films showed a relative motion of  $x \approx 25 \mu\text{m}$  after the samples had been processed, which is consistent with the film thickness and the strain extracted from the above model.

The effect of multiple-pass edge-shear processing is investigated in Figure 2c. The depth of the resonant minimum in fractional transmittance is parameterized as  $Q$ , which is given by the difference between the dip intensity and the shorter-wavelength transmission (Figure 2c, inset). This quality parameter of 3D order is seen to significantly improve, not only after the first pass of edge shear, but also with subsequent repeat passes at a speed of  $5 \text{ mm s}^{-1}$ . By comparison, the intensity and full width at half-maximum (FWHM) of the bright- and dark-field reflectance spectra improve markedly after the first-pass edge shear (Supporting Information, Figure S3), but do not significantly improve with subsequent passes. These results indicate that, remarkably, the surface ordering in the opal goes to near-completion on a single-pass of the hot-edge, whereas the bulk ordering may still be improved upon by repeated processing. To reconcile these observations, bright-field reflectance of the top and bottom surfaces is compared for increasing hot-edge passes (Figure 2d). After the linear shear (rolling) process, the bottom surface appears slightly more ordered than the top surface. However, a single pass of the hot-edge produces a much stronger structural color effect on the top surface than the bottom; we believe this is because the shearing forces are not uniform throughout the film, but are greatest on the top surface, which is furthest from the point of the hot-edge apex. Successive repeat passes then cause this color to improve on both sides, culminating in the top and bottom spectra being virtually identical after three passes. This confirms the progressive improvement in bulk-ordering across the full depth of the film upon repeated edge-shearing. While the quality  $Q$  is  $\approx 0.1$  for processing speeds of 2, 5, and  $10 \text{ mm s}^{-1}$ , it rapidly degrades for the broad spectra measured at speeds exceeding  $20 \text{ mm s}^{-1}$  (Supporting Information, Figure S3). Although structural color in surface reflectance is still present for faster processing speeds, the dynamics of shearing are too slow to develop full bulk ordering in  $\approx 100\text{-}\mu\text{m}$ -thick films at these processing temperatures.

Finally, we verify this model by considering the case of larger hot-edge apex angles. The model predicts that once the angle is too shallow, the reduced shear strain produced in the EIRS

process is insufficient to induce significant reordering. As the optical properties are tracked when the apex angle is increased from  $90^\circ$  to  $120^\circ$  and  $150^\circ$ , the bright-field reflectivity shows that beyond  $120^\circ$  the EIRS process loses its effectiveness, as expected from this analysis (Supporting Information, Figure S4). Further experiments, which are underway to study the effects of this angle and other variables of the processing in a more complete and systematic way, will refine the model quantitatively.

We anticipate being able to extend the methods described here into a much wider range of CIS systems, using polymers and polymeric composites such as metallo-dielectrics. The novel use of soft nanomaterials in the design of photonic structures, with macroscale bulk ordering, presents opportunities for a step-change away from the monolithic architectures that are currently relied upon, with the goal of key advances in the areas of organic optoelectronics and optical metamaterials. The unique structural color properties of polymeric opals, together with intrinsic processability, stretchability, and durability also make them attractive for mainstream applications, such as decorative coatings, fabrics,<sup>[25]</sup> security or antiforgery labeling, and in thermochromic indicators.<sup>[26]</sup>

## Experimental Section

**Sample Preparation:** As-synthesized batches of the CIS material, together with a small amount ( $<0.1 \text{ wt}\%$ ) of carbon-black powder ("Special Black 4", Degussa), were extruded into millimeter-sized ribbons using a twin co-rotating-screw mini-extruder at  $150^\circ\text{C}$ . In order to produce thin-film opaline samples, these ribbons were then encapsulated between 2-m-long, 4-cm-wide PET tapes, as illustrated in Figure 1b,c. The tapes were fed under a quartz roller, which had a compressive downwards pressure of 40 psi, and through a cartridge consisting of two brass capstans (to ensure positioning) and a polished brass hot-edge, with an apex angle of  $\alpha = 90^\circ$  and radius of curvature  $<10 \mu\text{m}$ . The sample was positioned on a heated glass plate, with the cartridge and plate preheated to  $150^\circ\text{C}$ . Firstly, the translation stage was moved horizontally at  $1 \text{ mm s}^{-1}$  relative to the roller, which was free to rotate, pressing the sample into uniform thin films in a squeeze/shear mechanism (Figure 1b). The roller was typically set to produce thicknesses on the order of  $100 \mu\text{m}$  and films of area  $10\text{--}20 \text{ cm}^2$ . Secondly, the PET tapes were secured at both ends and the translation stage was used to draw the thin-film tapes over the heated brass edge at typical speeds of  $5 \text{ mm s}^{-1}$ . This latter step was done as a single-pass or repeated several times in either direction.

For diffraction experiments, spectroscopy, and microscopy, see the Supporting Information.

## Supporting Information

Supporting Information is available from the Wiley Online Library or from the author.

## Acknowledgements

This work was supported by EPSRC (UK) grants EP/G060649/1, EP/E040241, EP/H027130/1. The authors thank Prof. M. Mackley of the University of Cambridge for very helpful discussions and R. Hardy of the Cavendish Laboratory for technical assistance.

Received: October 25, 2010

Revised: January 11, 2011

Published online:

- [1] B. J. Ackerson, P. N. Pusey, *Phys. Rev. Lett.* **1988**, *61*, 1033.
- [2] R. M. Amos, J. G. Rarity, P. R. Tapster, T. J. Shepherd, *Phys. Rev. E* **2000**, *61*, 2929.
- [3] R. de la Rue, *Nat. Mater.* **2003**, *2*, 74.
- [4] Y. A. Vlasov, X. Z. Bo, J. C. Sturm, D. J. Norris, *Nature* **2001**, *414*, 289.
- [5] P. Nagpal, N.C. Lindquist, S-H. Oh, D. J. Norris, *Science* **2009**, *31*, 594.
- [6] V. N. Astratov, A. M. Adawi, S. Fricker, M. S. Skolnick, D. M. Whittaker, P. N. Pusey, *Phys. Rev. B* **2002**, *66*, 165215.
- [7] A. A. Chabanov, Y. Jun, D. J. Norris, *Appl. Phys. Lett.* **2004**, *84*, 3573.
- [8] A. F. Koenderink, A. Lagendijk, W. L. Vos, *Phys. Rev. B* **2005**, *72*, 153102.
- [9] S. A. Asher, J. M. Weissman, A. Tikhonov, R. D. Coalson, R. Kesavamoorthy, *Phys. Rev. E* **2004**, *69*, 066619.
- [10] J. Ge, Y. Hu, Y. Yin, *Angew. Chem. Int. Ed.* **2007**, *46*, 7428.
- [11] O. L. J. Poursiainen, J. J. Baumberg, H. Winkler, B. Viel, T. Ruhl, *Appl. Phys. Lett.* **2005**, *87*, 101902.
- [12] O. L. J. Poursiainen, J. J. Baumberg, H. Winkler, B. Viel, P. Spahn, T. Ruhl, *Adv Mater.* **2008**, *20*, 1484.
- [13] D. R. E. Snoswell, A. Kontogeorgos, J. J. Baumberg, T. D. Lord, M. R. Mackley, P. Spahn, G. P. Hellmann, *Phys. Rev. E* **2010**, *81*, 020401.
- [14] O. L. J. Poursiainen, J. J. Baumberg, H. Winkler, B. Viel, P. Spahn, T. Ruhl, *Opt. Express* **2007**, *15*, 9552.
- [15] J. J. Baumberg, O. L. Poursiainen, P. Spahn, *Phys. Rev. B* **2009**, *80*, 201103.
- [16] P. Vukusic, J. R. Sambles, *Nature* **2003**, *424*, 852.
- [17] T. Ruhl, P. Spahn, G. P. Hellmann, *Polymer* **2003**, *44*, 7625.
- [18] B. Viel, T. Ruhl, G. P. Hellmann, *Chem. Mater.* **2007**, *19*, 5673.
- [19] P. Ossi, *Disordered Materials*, Springer-Verlag, Heidelberg, Germany, **2006**.
- [20] P. Mach, P. Wiltzius, M. Megens, D. A. Weitz, K-H. Lin, T. C. Lubensky, A. G. Yodh, *Europhys. Lett.* **2002**, *58*, 679.
- [21] M. D. Haw, W. C. K. Poon, P. N. Pusey, *Phys. Rev. E* **1998**, *57*, 6859.
- [22] F. García-Santamaría, J. F. Galisteo-López, P. V. Braun, C. López, *Phys. Rev. B* **2005**, *71*, 195112.
- [23] R. Abbaschian, L. Abbaschian, R. E. Reed-Hill, *Physical Metallurgy Principles*, 4th Edition, CL-Engineering, Stamford CT USA, **2008**.
- [24] A. Kontogeorgos, D. R. E. Snoswell, C. E. Finlayson, J. J. Baumberg, P. Spahn, G. P. Hellmann, *Phys. Rev. Lett.* **2010**, *105*, 233909.
- [25] C. E. Finlayson, C. Goddard, E. Papachristodoulou, D. R. E. Snoswell, A. Kontogeorgos, P. Spahn, G. P. Hellmann, O. Hess, J. J. Baumberg, *Opt. Express* **2011**, *19*, 3144.
- [26] J. Sussman, D. R. E. Snoswell, A. Kontogeorgos, J. J. Baumberg, P. Spahn, *Appl. Phys. Lett.* **2009**, *95*, 173116.